^{40}Ar/^{39}Ar Geochronological Constraints on the Age Progression Along the Juan Fernández Ridge, SE Pacific

Luis E. Lara[1]*, Javier Reyes[2,3], Brian R. Jicha[4] and Juan Díaz-Naveas[5]

[1] Servicio Nacional de Geología y Minería, Santiago, Chile, [2] Departamento de Geología, Facultad de Ciencias Físicas y Matemáticas, Universidad de Chile, Santiago, Chile, [3] Centro de Excelencia en Geotermia de los Andes, Santiago, Chile, [4] University of Wisconsin–Madison, Madison, WI, United States, [5] Escuela de Ciencias del Mar, Pontificia Universidad Católica de Valparaíso, Valparaíso, Chile

Juan Fernández Ridge (JFR) is a *ca.* 800 km long volcanic chain composed by seamounts, guyots and oceanic islands in the SE Pacific. JFR is thought to be related to a deep mantle plume and usually scores high in the hotspots catalogs (e.g., Anderson, 2005; Jackson et al., 2017). High ^{3}He/^{4}He in Robinson Crusoe is probably the most undoubted feature of lower mantle involvement. However, one of the most convincing pieces of evidence for a source rooted deep in the mantle is the age progression along a volcanic chain, which is poorly constrained for JFR. In fact, some scarce K-Ar dates in Alejandro Selkirk and Robinson Crusoe islands, and a total fusion age for O'Higgins Guyot published more than 20 years ago, is the only evidence available for such a hypothesis in previous works. Here we integrate recently published ^{40}Ar/^{39}Ar ages and 17 new results on groundmass step heating experiments from rocks corresponding to the late shield stage (O'Higgins Guyot: 8.4 Ma; Alpha Guyot: 4.6 Ma; Robinson Crusoe Island: 3.7 Ma; Alejandro Selkirk Island: 0.83 Ma; Friday Seamount: 0.62 Ma) to document a solid age progression which yields a long-term absolute velocity of *ca.* 81 mm/year$^-$ for the Nazca Plate. This value is much higher than the velocity prescribed by plate tectonic models that assume fixed hotspots, and still somewhat higher than models that take into account hotspot drift, indicating that the Juan Fernández hotspot is moving *ca.* 20 mm/year toward East Pacific Rise. Present hotspot would be *ca.* 20 km west of Domingo Seamount. Merging geochronological data with our current understanding of the mantle sources and magmatic evolution, we provide a case for a hotspot possibly rooted in a weak primary plume, and discuss some causes and consequences of that.

Keywords: seamounts, guyots, mantle plumes, Juan Fernández Ridge, SE Pacific

INTRODUCTION

Seamounts are conspicuous features of the deep seafloor, and together with oceanic islands, form a widespread expression of intraplate volcanism. Linear arrays of seamounts, some of them forming age progressive trails of intraplate volcanoes were early described from the Hawaiian chain by McDougall (1964, 1971) based on K-Ar geochronology. From that

finding emerged the fixed hotspot concept (e.g., Wilson, 1963; Morgan, 1971, 1972) with a remarkable and long-lasting influence on plate tectonics and modern geodynamics. However, in the last decades more detailed global bathymetry has revealed more seamounts in a wide range of size and geometry, many of them isolated and others forming chains with no clear age progression. The latter became evident for the Pacific basin (Clouard and Bonneville, 2001) and thus new ideas were raised to question the fixed hotspot model, and the mantle plumes theory. Bonatti et al. (1977) early proposed the "hot lines" as a kind of leaky fractures controlling linear arrays. Lithosphere cracking was proposed by Sandwell and Fialko (2004) whereas Ballmer et al. (2007) proposed the small-scale sublithospheric convection as a way to form long chains that violate the age progression expected for fixed hotspots. A milestone in testing age progressions is geochronology, and the advent of ^{40}Ar/^{39}Ar geochronology with modern spectrometers opened avenues to study these features with growing accuracy.

A suitable target for this kind of study is the Juan Fernández Ridge (JFR) in the SE Pacific, close to the south-eastern corner of the so-called Pacific Large-Low Shear Velocity Province (Steinberger and Torsvik, 2012). JFR is thought to be related to a deep mantle plume and usually scores high in the hotspots catalogs (e.g., Anderson, 2005; Jackson et al., 2017), mostly because of high ^{3}He/^{4}He ratios in Robinson Crusoe Island, but firm geochronology is still lacking. In fact, some scarce K-Ar dates for Alejandro Selkirk and Robinson Crusoe islands (Booker et al., 1967; Stuessy et al., 1984) and a total fusion ^{40}Ar/^{39}Ar age for O'Higgins Guyot published more than 20 years ago (von Huene et al., 1997) is the only evidence available for such a hypothesis. In addition, JFR seems to be also important for the evolution of the South American continental margin. In fact, the intersection of the JFR with the continental margin coincides with the southern limit of the Pampean flat slab (Ramos et al., 2002; Ramos and Folguera, 2009) and is the starting point for high sedimentation rates at the trench (von Huene et al., 1997) and hence is thought to be playing a role on the segmentation of the margin and to control processes in the overriding plate (Kay et al., 1991; Reich et al., 2003; Le Roux et al., 2005; Rosenbaum and Mo, 2011; Arriagada et al., 2013). Therefore, a better understanding of the nature and specially timing of the JFR collision would shed light on some of those relevant margin-scale processes.

Here we use ^{40}Ar/^{39}Ar geochronology on groundmass, whole rock and plagioclase separates to date shield stage lavas along the JFR, and by comparison with other age-progressive seamount chains on the Nazca Plate (e.g., Easter Seamount Chain, ESC), we discuss their origin in the context of mantle plumes and plate tectonics.

REGIONAL TECTONIC SETTING

The JFR intersects the continental margin at ∼33.4°S and its eastern component (O'Higgins seamounts group) is located ∼120 km west of the Chile-Peru Trench (**Figure 1**), where the Nazca Plate sinks beneath South America with an azimuth of 78.4° at a high convergence rate of 74 mm/year according to

the MORVEL model (DeMets et al., 2010) or 70.5 mm/year according to the GEODVEL 2010 model (Argus et al., 2010). The age of the Nazca Plate underneath the JFR ranges from 27 to 37 Ma (Müller et al., 2008) and is segmented by the Challenger Fracture Zone, which defines a conspicuous magnetic domain that disrupts the normal pattern of the oceanic plate and cuts the JFR near Robinson Crusoe Island (Rodrigo and Lara, 2014). South of the Challenger Fracture Zone, the oceanic crust of the Nazca Plate forms at the Chile Ridge whereas its northern domain is originated at the fast spreading East Pacific Rise (Cande and Haxby, 1991). The Challenger Fracture Zone is EW-trending at the Chile Ridge but changes to a more oblique ENE strike near the Selkirk trough, south of the JFR (**Figure 1**). Close to the JFR, the Challenger Fracture Zone is poorly defined but appears as a sharp discontinuity of the magnetic fabric (Rodrigo and Lara, 2014). 3D modeling of the magnetization suggests that the fracture zone would also have channelized intrusions in a trend that departs from the JFR (Rodrigo and Lara, 2014).
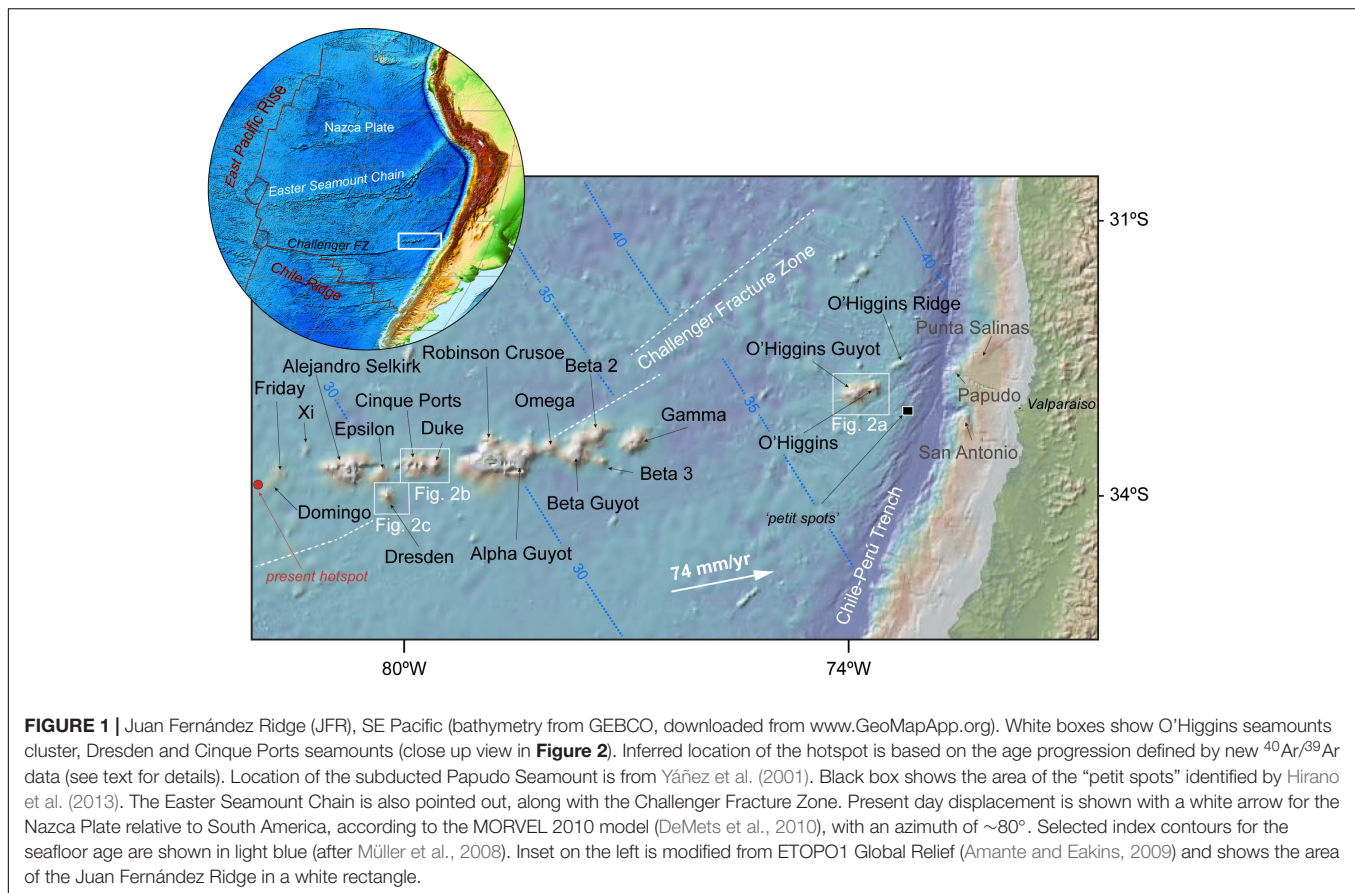
Global bathymetry based on satellite altimetry (Weatherall et al., 2015; GEBCO 2014 at www.GeoMapApp.org) shows the JFR to be a *ca.* 800 km long EW-trending chain that extends eastward from the Friday and Domingo seamounts (at 97.5°W/34°S, close to where the present hotspot would be located; e.g., von Huene et al., 1997) nearly parallel to the convergence vector. The JFR has a roughly continuous morphology west of 76.5°W (Gamma Seamount), where a free air gravity response can be observed (Yáñez et al., 2002; Tassara et al., 2006). Negative anomalies along the flanks define a moat structure as expected by flexural loading of the oceanic crust. Beyond a bathymetric gap, this signature is not evident further east where the gravimetric anomaly is centered at the O'Higgins seamounts cluster without a resolved moat structure (Flueh et al., 2002; Kopp et al., 2004). The latter has been interpreted as the absence of a crustal root, although a broader feature could be masked by the Nazca Plate bending at the outer-rise (Kopp et al., 2004).

Long-term effects of the collision of JFR against the continental margin have been extensively proposed in terms of tectonics (e.g., Yáñez et al., 2002; Le Roux et al., 2005; Arriagada et al., 2013), magmatism (Kay et al., 1991) and even mineral resources (e.g., Reich et al., 2003), although based on the existing poor geochronology and an arguable geometry of the subducted portion of the ridge (Yáñez et al., 2001). In fact, the NE- bending of the trail at *ca.* 25–26 Ma proposed by Yáñez et al. (2001) implies a rapid southward migration of the ridge collision point for ∼1400 km since 22 Ma to a more orthogonal encounter at 10 Ma, when the EW segment started to subduct.

MATERIALS AND METHODS

^{40}Ar/^{39}Ar Geochronology

Eleven ^{40}Ar/^{39}Ar laser incremental heating experiments were conducted at the WiscAr Geochronology Laboratory using both MAP 215-50 and Noblesse 5-collector mass spectrometers. Groundmass separates were prepared by crushing, sieving to 250–355 µm, magnetic sorting, and density separation

FIGURE 1 | Juan Fernández Ridge (JFR), SE Pacific (bathymetry from GEBCO, downloaded from www.GeoMapApp.org). White boxes show O'Higgins seamounts cluster, Dresden and Cinque Ports seamounts (close up view in **Figure 2**). Inferred location of the hotspot is based on the age progression defined by new ^{40}Ar/^{39}Ar data (see text for details). Location of the subducted Papudo Seamount is from Yáñez et al. (2001). Black box shows the area of the "petit spots" identified by Hirano et al. (2013). The Easter Seamount Chain is also pointed out, along with the Challenger Fracture Zone. Present day displacement is shown with a white arrow for the Nazca Plate relative to South America, according to the MORVEL 2010 model (DeMets et al., 2010), with an azimuth of ∼80°. Selected index contours for the seafloor age are shown in light blue (after Müller et al., 2008). Inset on the left is modified from ETOPO1 Global Relief (Amante and Eakins, 2009) and shows the area of the Juan Fernández Ridge in a white rectangle.

using methylene iodide. The separates were then ultrasonically leached as needed in a 5–10% HCl, rinsed ultrasonically with deionized water, and then hand-picked under a binocular microscope to remove altered domains. Groundmass separates, along with the 28.201 Ma Fish Canyon sanidine standard (Kuiper et al., 2008) or the 1.18 Ma Alder Creek rhyolite sanidine (Jicha et al., 2016), were irradiated at the Oregon State University TRIGA reactor in the Cadmium-Lined In-Core Irradiation Tube (CLICIT). Groundmass separates of ∼20 mg were incrementally heated with a 25 W CO_2 laser following the procedures in Jicha and Brown (2014) and analyzed using the MAP 215-50 single collector mass spectrometer. Youngest sample 'FRIDAY' was incrementally heated with a 60 W CO_2 laser and analyzed using a Noblesse 5-collector mass spectrometer following the procedures in Jicha et al. (2016). Reported ages in **Table 2** were calculated using the decay constants of Min et al. (2000) and analytical uncertainties, including J contributions (neutron fluence monitor during irradiation), are reported at the 95% confidence level ($\pm$ 2σ).

Nine samples (**Table 2**) were analyzed by ^{40}Ar/^{39}Ar laser incremental heating at the SERNAGEOMIN Geochronology Laboratory using a MAP 215-50 mass spectrometer. Fresh rock fragments were crushed to 250–180 μm grain sizes and hand-picked to extract major phenocrysts or weathered surfaces. Single aliquots were placed in a disk of high purity aluminum together

with a monitor grain of Fish Canyon sanidine (28.03 ± 0.1 Ma; Renne et al., 1994). Sealed disk was sent for irradiation to La Reina nuclear reactor (Chile), operated by the Comisión Chilena de Energía Nuclear. Samples were irradiated for 20 h. Once the samples were received from the reactor, individual total fusion analyses were performed for all the monitors from the disk, and J factors were calculated for each grain. The distribution of J in 2 dimensions across the disk is modeled by a 2-dimensional quadratic fit to the data, resulting in a J surface for the disk (e.g., Lara et al., 2006 and references therein). Individual J factors for each sample are thus calculated depending upon the coordinates of the sample. Following each three heating steps a line blank was analyzed. Then, the noble gases were separated by means of a cold trap at ≈133°C and a ST101 getter operated at 2.2 A. Once purified, the noble gases were introduced into a high resolution MAP 215-50 mass spectrometer in electron multiplier mode. The isotopes ^{36}Ar, ^{37}Ar, ^{38}Ar, ^{39}Ar, and ^{40}Ar were analyzed in 10 cycles, and the ^{36}Ar/^{40}Ar, ^{37}Ar/^{40}Ar, ^{38}Ar/^{40}Ar, and ^{39}Ar/^{40}Ar ratios were calculated for time zero to eliminate the effects of isotope fractionation during the analysis. The baseline was analyzed at the beginning and the end of the analysis, for each step, and subtracted from the peak heights. Spectrometer bias was corrected using periodic analyses of air samples, from which a correction factor was calculated. A reproducible result was considered when a plateau age was defined using the approach

TABLE 1 | Morphological features and inferred ages along the JFR.

Seamount/Island	Lat (°S)	Long (°W)	Vol (km³) (eroded)	Age (Ma)* ± 2σ		Crust age ± 0.5 (Ma) Muller et al. (2008)	Δage ± 1 (Ma)	Comments	Relevant references
Punta Salinas Ridge	32 25.00′	72°05.00′	-	10.74	0.50	39.4	28.7	Subducted, no reliable volume estimation	Yáñez et al., 2001
San Antonio Seamount	33 05.00′	72°05.00′	-	10.59	0.50	38.8	28.2	Subducted, no reliable volume estimation	Laursen and Normark, 2002
Papudo seamount	32°36.00′	72°30.00′	380	10.23	0.50	38.8	28.6	Subducted; volume from magnetic anomaly	Yáñez et al., 2001
O'Hiigins ridge	32°34.71′	73°18.24′	345	*9.42*	*0.50*	37.6	28.2	Age inferred from age progression	von Huene et al., 1997
O'Higgins seamount	32°53.80′	73°50.10′	380	*9.02*	*0.50*	36.9	27.9	Age inferred from age progression	von Huene et al., 1997
O'Higgins (Guyot)	32°54.16′	73°54.17′	1305	8.64	0.28	36.5	27.9	^{40}Ar/^{39}Ar geochronology	Lara et al., 2018
Gamma	33 27.28′	76°51.91′	2400	*5.59*	*0.50*	32.2	26.6	Age inferred from age progression	
Beta 3	33 41.05′	77°20.10′	400	*5.07*	*0.50*	31.4	26.3	Age inferred from age progression	
Beta 2	33 23.14′	77°27.08′	1100	*5.00*	*0.50*	31.5	26.5	Age inferred from age progression	
Beta (Guyot)	33 37.54′	77°43.56′	3000	*4.68*	*0.50*	31.1	26.4	Age inferred from age progression	
Omega	33 31.93′	78°02.55′	700	*4.37*	*0.50*	30.8	26.4	Age inferred from age progression	
Alfa (Guyot)	33 40.50′	78°28.59′	4300	3.91	0.06	30.3	26.4	^{40}Ar/^{39}Ar geochronology	
Robinson Crusoe	33 38.26′	78°51.48′	7600	3.52	0.11	30,0	26.5	^{40}Ar/^{39}Ar geochronology	Booker et al., 1967; Stuessy et al., 1984; Baker et al., 1987; Reyes et al., 2017
Duke	33 43.68′	79°36.94′	1600	*2.73*	*0.50*	29.7	27.0	Age inferred from age progression	Rodrigo and Lara, 2014
Cinque Ports	33 44.89′	79°52.28	1600	*2.47*	*0.50*	29.5	27.0	Age inferred from age progression	Rodrigo and Lara, 2014
Dresden	34 04.91′	80°15.70′	600	*2.06*	*0.50*	28.9	26.8	Age inferred from age progression	Rodrigo and Lara, 2014
Epsilon	33 49.61′	80°20,94′	750	*1.96*	*0.50*	29.2	27.2	Age inferred from age progression	
Alejandro Selkirk	33 45.66′	80°47.22′	4800	*1.54*	*0.10*	28.7	27.2	^{40}Ar/^{39}Ar geochronology	
Xi	33 34.57′	81°22.41′	150	*1.09*	*0.50*	28.6	27.5	Age inferred from age progression	
Friday	33 47,40′	81°43.50′	600	*0.66*	*0.50*	28.4	27.7	^{40}Ar/^{39}Ar geochronology	Farley et al., 1993
Domingo	33 56.80′	81°50.70′	320	*0.42*	*0.50*	28.2	27.8	Age inferred from age progression	Devey et al., 2000

Ages reported in italics are from the regression line (see text for details). Age of the seafloor taken from Muller et al. (2008) in GeoMapApp, with a nominal maximum uncertianty of 0.5 Ma. Δage is the difference between Age and Crust age with 1 Ma of nominal uncertainty. Volumes estimated from the best bathymetry available, mostly from GRMT in GeoMapApp, or published sources, with nominal uncertainty of 10%. Higher discrepancy is expected for guyots.

of Fleck et al. (1977) and Sharp and Renne (2005). Reported ages were calculated with the decay constants published by Steiger and Jagger (1977).

In order to obtain comparable values, we recalculated the age and uncertainties following the procedures by Mercer and Hodges (2016) using ArAR software tool[1], with the age published by Kuiper et al. (2008) for the Fish Canyon sanidine (28.201 Ma) and the decay constants of Min et al. (2000). **Table 2** contains

---

[1]http://group18software.asu.edu

TABLE 2 | Summary of $^{40}Ar/^{39}Ar$ incremental heating results of volcanic rocks from JFR shield stage.

Sample	Phase	K/Ca Total	Total Fusion	Isochron analysis			Age spectrum				Lab ref
			Age (Ma) ± 2σ	$^{40}Ar/^{39}Ar_I$ ± 2σ	Age (Ma) ± 2σ	N	MSWD	^{39}Ar (%)	Age (Ma) ± 2σ		
O'Higgins Guyot											
D10-2	GM	0.025	8.40 0.20	295.4 2.1	8.41 0.08	8 of 8	0.41	100	**8.41 0.07**	1	Lara et al., 2018
D10-7	GM	0.054	8.99 0.52	301.8 6.4	6.46 2.47	8 of 10	0.88	93.8	8.97 0.52		
	GM	0.061	9.12 0.35	296.0 3.9	9.20 1.39	14 of 22	0.8	88.5	9.28 0.33	2	This study
Weighted mean plateau and isochron ages:				8.50 1.20		22 of 32			**9.26 0.28**	2	This study
Alpha Guyot											
D11-03	GM	0.304	4.54 0.11	292.6 4.3	4.63 0.11	8 of 8	0.82	100	**4.58 0.06**	1	This study
D11-04	GM	0.191	4.64 0.07	294.4 15.9	4.64 0.14	8 of 8	0.23	100,0	**4.63 0.06**	2	This study
Robinson Crusoe Island											
MP270112-4	GM	0.218	3.64 0.07	281.1 18.7	3.82 0.20	6 of 10	0.81	94.5	3.67 0.06		
	GM	0.222	3.72 0.10	319.3 36.1	3.52 0.36	7 of 9	1.24	91.7	3.75 0.1		
Weighted mean plateau and isochron ages:				3.75 0.17		13 of 19			**3.70 0.05**	2	This study
JR220112-2	GM	0.175	3.78 0.04	294.4 3.9	3.82 0.05	7 of 9	0.71	91.7	**3.81 0.04**	2	This study
LL240711-1	GM	0.002	3.80 0.06	296.0 3.0	3.79 0.04	7 of 7	1.17	100,0	3.79 0.04		
	GM	0.012	3.82 0.06	294.0 2.0	3.85 0.04	7 of 7	1.17	100,0	3.85 0.03		
Weighted mean plateau and isochron ages:				3.83 0.03		14 of 14			**3.83 0.03**	1	Reyes et al., 2017
LL230112-1	GM	0.152	3.47 0.28	292.9 2.4	4.07 0.33	10 of 13	1.05	89,0	3.79 0.22		
	GM	0.147	3.67 0.38	293.8 2.1	4.08 0.29	8 of 8	0.69	100,0	3.91 0.21		
Weighted mean plateau and isochron ages:				4.08 0.22		18 of 21			**3.85 0.15**	2	This study
MP260112-1	GM	0.123	3.85 0.06	293.2 3.5	3.90 0.06	11 of 11	0.92	100,0	**3.87 0.05**	2	This study
LL250711-8	WR	0.025	3.85 0.06	294.0 6.0	3.89 0.06	7 of 7	1.45	100,0	3.89 0.03		
	WR		3.87 0.10	297.0 3.0	3.85 0.08	7 of 7	0.07	100,0	3.86 0.06		
Weighted mean plateau and isochron ages:				3.88 0.04		14 of 14			**3.87 0.04**	1	This study
LL260711-2	WR	0.023	3.94 0.07	296.0 2.0	3.94 0.02	7 of 7	0.48	100,0	3.94 0.02		
	WR	0.015	3.98 0.09	296.0 3.0	3.97 0.03	7 of 7	0.76	100,0	3.97 0.02		
Weighted mean plateau and isochron ages:				3.95 0.02		14 of 14			**3.96 0.02**	1	This study
JR220112-1	Plag	0.045	3.7 0.5	296.6 54.5	3.41 0.59	7 of 7	0.69	100	**3.40 0.30**	1	This study
LL250711-5	GM	0.094	3.73 0.15	307.9 31.9	3.69 0.31	8 of 9	0.61	96.7	3.8 0.12		
	GM	0.096	3.72 0.12	286.0 20.0	3.89 0.23	6 of 8	1.08	95.9	3.79 0.11		
Weighted mean plateau and isochron ages:				3.82 0.19		14 of 17			**3.80 0.08**	2	This study
LL270711-5	GM	0.752	4.12 0.11	295.6 2.2	4.09 0.15	10 of 12	0.77	95.8	**4.10 0.09**	2	This study
Alejandro Selkirk Island											
LL270112-2	GM	0.22	0.98 0.07	301.6 34.0	0.89 0.23	9 of 11	0.47	90,0	**0.94 0.07**	2	This study
JR170913-16	GM	0.173	0.84 0.13	295.3 1.8	0.83 0.04	8 of 8	0.21	100	**0.83 0.03**	1	This study
LL260913-4	GM	0.185	1.00 0.10	266.4 51.1	1.11 0.19	8 of 9	0.93	99.5	1.01 0.08		
	GM	0.191	0.90 0.02	291.1 20.4	0.94 0.07	6 of 8	1.15	97,0	0.92 0.02		
Weighted mean plateau and isochron ages:				0.96 0.07		14 of 17			**0.93 0.02**	2	This study
JR180913-1	GM	0.104	0.87 0.02	243.3 5.0	0.88 0.02	7 of 7	0.63	100,0	**0.88 0.01**	1	This study
JR170913-7	WR	8407,000	0.93 0.06	294.1 3.6	0.93 0.02	7 of 7	0.3	100,0	**0.93 0.02**	1	This study
Friday											
FRIDAY	GM	0.143	0.59 0.13	296.3 3.6	0.97 0.91	16 of 16	1.08	100,0	**0.62 0.13**	2	This study

(1): SERNAGEOMIN Geochronology Laboratory, www.sernageomin.cl. (2): University of Wisconsin–Madison, WiscAr Laboratory, https://geochronology.geoscience.wisc.edu. GM, groundmass; WR, whole rock; Plag, plagioclase. MSWD is the mean standard weight deviation. Values in bold are preferred ages.

values as reported from the laboratories and a column with the recalculated values. Subsequent figures use corrected values.

Geological Mapping, Bathymetry and Sampling

Most dated samples come from the islands, and for them exist stratigraphic constraints on relative ages based on 1:25,000 scale geological mapping. Some others were dredged during cruises since 1995. Global low resolution bathymetry (e.g., Global Multi Resolution Topography at www.GeoMapApp.org) was used for first-order geomorphological analysis, complemented with multibeam surveys in the area, for example the Hydrosweep mapping of SO101 CONDOR cruise in 1995 (von Huene et al., 1997) and multibeam bathymetry of SO161 SPOC campaign in 2000 (Flueh et al., 2002; Reichert and Schreckenberger, 2002). Higher resolution bathymetric charts were produced with multibeam echosounders Kongsberg EM122 (12 kHz) and EM710 (70–100 kHz) on board of the AGS 61 Cabo de Hornos research vessel during the FIPA (Fondo de Investigación Pesquera y de Acuicultura) cruise in July 2014, mostly for Duke, Cinque Ports and Dresden seamounts (as named by Rodrigo and Lara, 2014). MB-System software (Caress and Chayes, 2017) was used for post-processing and GMT software (Wessel and Smith, 1995) served to prepare interpolation grids with 30 m of horizontal resolution for the whole depth range and with 6 m at seamounts summits (depth range from 300 to 1000 m). From the available bathymetry, seamount volumes were estimated from sections in which we identified basal planes as those where curvature change is maximum, and after assuming simple geometries for calculation purposes. We assign a nominal uncertainty of *ca.* 20% as a very conservative value for volume estimations, which also takes into account uncertainty related to erosion and total growth above sea level.

Geochemistry

In this article we briefly discuss the main geochemical signatures of the JFR rocks extensively described in Reyes et al. (2017), Reyes (2018, unpublished), and Lara et al. (2018), where methods and procedures for whole rock and mineral geochemistry are described in detail. We focus here on the shield stage because it is the main building stage with a long-term plumbing system (Reyes et al., 2017) and thus could provide clues about the nature of the underlying mantle source. There is evidence of a rejuvenated stage at O'Higgins Guyot (Lara et al., 2018) and Robinson Crusoe Island (Reyes et al., 2017) but we do not further discuss about its origin or driving factors. A discussion of the contrasting patterns of ascent and magmatic evolution between shield and rejuvenated stage lavas in JFR can be found in Reyes et al. (2017). Ongoing research about the mantle source of JFR magmas includes Sr-Nd-Pb isotope ratios and systematic modeling of the melting process. Whole rock major and trace elements here discussed were analyzed at AcmeLabs, Vancouver, BC, Canada[2]. Rock chips crushed from field hand samples were fused with lithium metaborate/tetraborate followed by a dilute nitric acid digestion prior to major element analysis by ICP-ES and trace elements

[2]www.acmelab.com

by ICP-MS. In addition, a separate split was digested in Aqua Regia and analyzed by ICP-MS to report the precious and base metals content. Loss on ignition (LOI) is determined by weight difference after ignition at 1000°C. Precision and accuracy (2σ) is between 3–8% for all elements (in ICP-ES and ICP-MS).

JUAN FERNÁNDEZ RIDGE

Seamounts and Islands Along the JFR

The JFR is composed of more than 20 seamounts, a number of knolls and two main islands (Rodrigo and Lara, 2014 and references therein) emplaced on the Nazca Plate. JFR converges against the South American Plate at ∼33.4°S (**Figure 1**). An already subducted portion of this ridge was identified by magnetic anomalies (von Huene et al., 1997; Yáñez et al., 2001), the most prominent depicting the Papudo Seamount (von Huene et al., 1997), which has a volume of *ca.* 380 km[3], comparable to the O'Higgins Seamount further west (**Table 1**). On the overriding plate a tectonic fabric develops in response to the JFR subduction, the ENE-trending Punta Salinas Ridge being one of the more clear expressions (von Huene et al., 1997). Normal and thrust faults are widespread and subsidence of the Valparaiso basin is interpreted as a consequence of the collision (Laursen et al., 2002). Structural highs are controlled by a complex pattern of contractional structures possibly underlain by subducted seamounts, such as the Topocalma knoll well above San Antonio Seamount (Laursen and Normark, 2002). This oblique structural fabric is partially aligned with that of the O'Higgins seamounts cluster in the outer-rise region on the Nazca Plate (**Figure 1**).

The JFR comprises two volcanic segments separated by a ∼400 km wide gap with a common base at *ca.* 3900 m depth. The Easter group is located 120 km west of the trench and is composed by the O'Higgins seamounts (**Figure 2**): O'Higgins Guyot, O'Higgins Seamount, O'Higgins Ridge and a number of knolls. Although they seem to be part of the roughly EW trend of the western JFR segment, they actually form a ENE-trending (N70°E) alignment subparallel to the fault pattern of the incoming plate observed in this region (**Figure 2**; Laursen et al., 2002; Ranero et al., 2006). This structural feature, orthogonal to the magnetic fabric, is notably marked by the O'Higgins fault (Kopp et al., 2004), a deep scarp south of the O'Higgins Guyot but also by the elongation of the O'Higgins Ridge. The eastward projection of the O'Higgins group, however, still follows a more EW trend with the subducted Papudo Seamount (Yáñez et al., 2001) and maybe others inferred from the bulges in the marine forearc sequences. Laursen and Normark (2002) interpreted the structural high south of the Valparaiso basin as a consequence of the accretion of the San Antonio Seamount. O'Higgins Ridge is a ∼45 km long elongated feature composed by a number of juxtaposed seamounts, flanked by extremely deep fractures (von Huene et al., 1997; Ranero et al., 2006). The O'Higgins Guyot is a volcanic edifice *ca.* 3450 m high with a flat top at *ca.* 500 mbsl on average, which is overlain by a rejuvenated lava flow (Lara et al., 2018). A total eroded volume of *ca.* 1300 km[3] was inferred for the O'Higgins Guyot (Lara et al., 2018). Maximum volume estimated using the formulas by Vogt and Smoot (1984) and
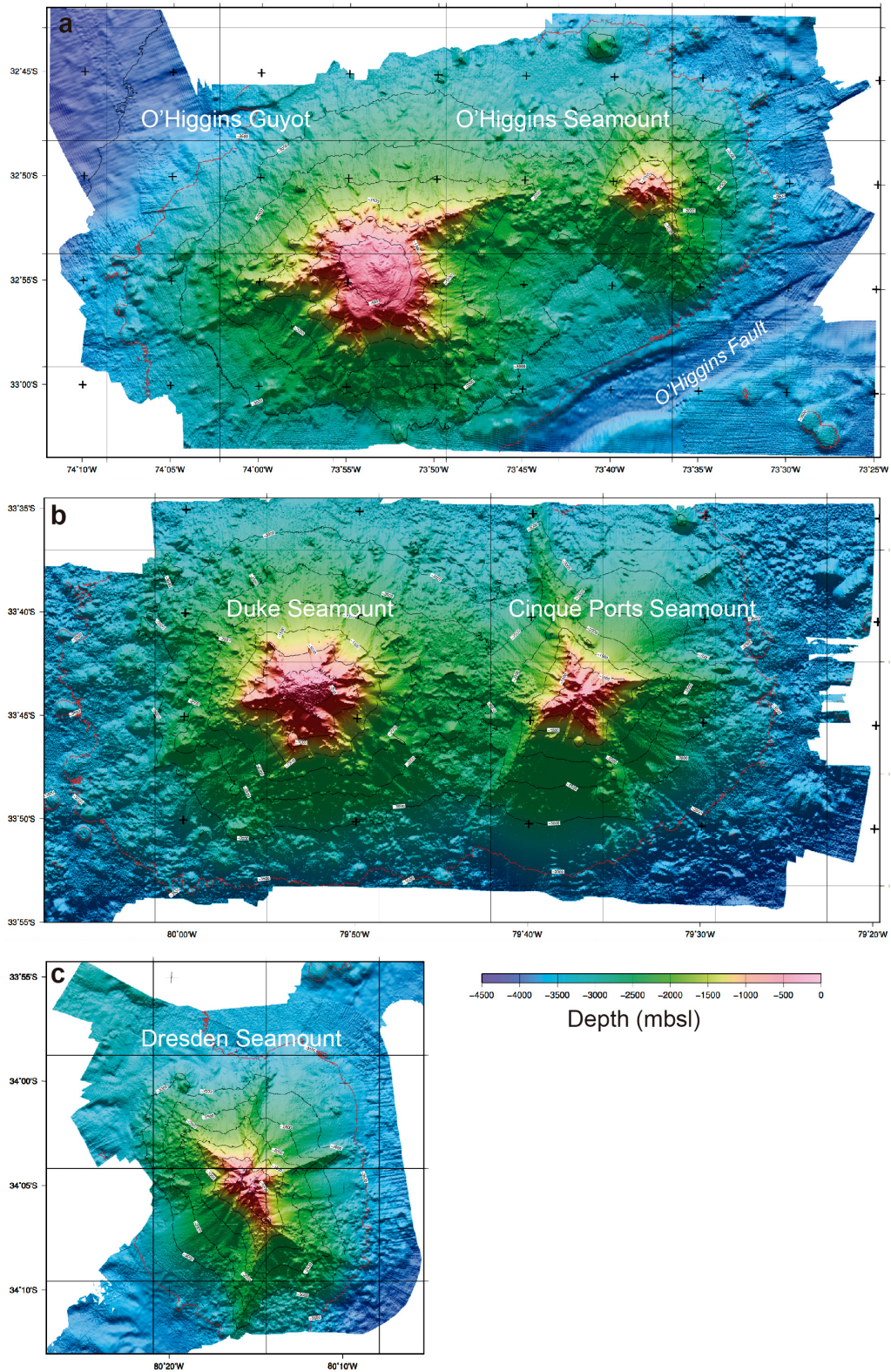
FIGURE 2 | Close up view for seamounts labeled in **Figure 1**. Contrasting morphologies (interpreted as different erosion degree) suggest a more complex evolution, despite the highly correlated linear trend described by geochronological data (see text for discussion). **(a)** O'Higgins cluster with O'Higgins Guyot and O'Higgins Seamount; **(b)** Duke, and Cinque Ports seamounts; **(c)** Dresden Seamount.

Mitchell (2001) is higher, within the range of uncertainty. The shelf break is partially obscured by the rejuvenated features. The summit cone is a compound structure *ca.* 2 km in diameter with a nested crater 930 m wide. From thickness estimated in bathymetric profiles a maximum volume of *ca.* 1.7 km^3 of rejuvenated basanites was deduced. The O'Higgins Seamount is a compound structure formed by two coalescent edifices with summits separated by 25 km with a saddle at *ca.* 2000 mbsl. Two $^{40}Ar/^{39}Ar$ groundmass ages of 9.26 ± 0.28 and 8.41 ± 0.07 were obtained by Lara et al. (2018), which are similar within uncertainty to the 8.5 ± 0.4 Ma total fusion age reported by von Huene et al. (1997). Above the summit plateau, a fresh and chemically distinctive rejuvenated lava flow was reported by Lara et al. (2018), with a groundmass age of *ca.* 8.2 Ma. The partially stellate edifice O'Higgins Seamount is *ca.* 3280 m high, has the summit at 720 mbsl and a present volume of *ca.* 380 km^3. About 45 km south of the O'Higgins Guyot, Hirano et al. (2013) reported two so-called "petit spots" (small seamounts sourced in the upper mantle and related to plate flexure, as defined in Hirano et al., 2006) dated at *ca.* 7–10 Ma.

The western segment is a nearly continuous ridge (N85°E) from Gamma to Domingo and includes 22 seamounts partially overlapping, 15 of them taller than 1000 m above seafloor. Gamma Seamount is a compound structure marking the resumption of volcanism after a ∼300 km gap. It is NE-elongated and has two summits, the shallowest at *ca.* 547 mbsl. A saddle at 3700 mbsl separates Gamma from the Beta seamounts cluster. Beta 2 is an apparently nested structure with a central cone at 700 mbsl and a total height of 2870 m. Beta 3 is a small perfect cone 1900 m high with a summit at 2020 mbsl, connected with Beta and Beta 2 through a saddle at 3000 mbsl. Beta is a prominent guyot with its flat surface only 250 mbsl and a total volume of *ca.* 3000 km^3. Beta and Beta 2 form a corridor joined by an unresolved bathymetric high, maybe representing another seamount. Omega Seamount, a perfect cone 2200 m high, is the bridge between Beta cluster and the large Alpha volcanic complex. The latter is a guyot with its flat surface gently dipping to the north, at 260–450 mbsl. A volume of *ca.* 4300 km^3 is inferred for this structure, which partially overlaps with the pedestal of Robinson Crusoe Island.

Robinson Crusoe Island (915 masl) and the nearby Santa Clara (375 masl) are part of the same edifice. Their advanced erosion exposes a continuous sequence of shiled stage lavas (Baker et al., 1987; Farley et al., 1993; Reyes et al., 2017; Truong et al., 2018). Submerged marine abrasion terraces (at ∼ 200 and ∼ 500 mbsl; Astudillo, 2014) and sedimentary layers of marine origin now uplifted at 70 masl indicate a complex history of vertical displacement (Sepúlveda et al., 2015). K-Ar ages of *ca.* 3.5–3.8 Ma (Booker et al., 1967; Stuessy et al., 1984) were later refined with a $^{40}Ar/^{39}Ar$ age of 3.83 ± 0.03 Ma by Reyes et al. (2017) for a tholeiitic basalt from the Puerto Inglés shield sequence. Rejuvenated volcanism is also present in Robinson Crusoe complex as pyroclastic cones, dykes and associated lavas. A sharp erosion unconformity separates the shield stage sequence from the younger rejuvenated stage (**Figure 3**). A basanite lava flow from the Bahía del Padre rejuvenated sequence was dated by Reyes et al. (2017) in *ca.* 0.9 Ma.

A saddle at *ca.* 3500 mbsl separates Robinson Crusoe Island from the paired Cinque Ports and Duke seamounts 70 km west (**Figure 2**; Rodrigo and Lara, 2014). Duke Seamount has a stellate form with a summit at *ca.* 500 mbsl and a height of *ca.* 3500 m (**Figure 2**). Four radial rift zones are recognized in the flanks, which appear also dotted by small flank vents. The western slope of Duke Seamount overlaps with the Cinque Ports Guyot, whose summit is 25 km west. Rough topography on the lower flanks could be interpreted as mass wasting deposits from sector-collapses. Cinque Ports is a guyot with its summit plateau at *ca.* 440 mbsl, with a height of 3660 m. Notably, a number of small cones are present at the base of the western flank, some of them with resolved craters. They are small 100–300 m high cones with diameters of 2–3 km. Five kilometers further west, Delta Seamount is an isolated small cone with summit at 1954 mbsl and base at 3565 mbsl. About 30 km south of the main alignment, Dresden Seamount appears as a stellate cone with a summit 380 mbsl and a height of 3620 m. It is elongated in the NW-SE direction and presents three prominent rift zones, one of them sigmoidal. North of Dresden Seamount, in the main alignment, is Epsilon Seamount, which is a dome-shaped edifice with a summit at *ca.* 1960 mbsl and a base at *ca.* 3570 mbsl.

Separated from Epsilon by a short saddle, Alejandro Selkirk Island is the other emergent volcanic edifice, ∼180 km W of Robinson Crusoe, with a summit 1320 masl and *ca.* 3800 m of submerged section. The sequence is exposed inland as a homoclinal sequence dissected by straight valleys downward to the east and high cliffs on the west coast. For Alejandro Selkirk the published K-Ar ages range between 2.44 and 0.85 Ma, with most of them *ca.* 1.0–1.3 Ma (Booker et al., 1967; Stuessy et al., 1984).

In the saddle that separates Alejandro Selkirk platform from the Domingo Seamount and Friday complex emerges the isolated Xi Seamount, a small perfect cone *ca.* 1000 m high. Further west, Friday (Farley et al., 1993) and Domingo (Devey et al., 2000) seamounts form a cluster with unresolved additional centers included. Friday complex has a multiple summit area at *ca.* 2900 mbsl with the base in the abyssal plain at *ca.* 3800 mbsl. Domingo is volumetrically smaller with a height of *ca.* 636 m. West of Domingo and Friday cluster there is a flat area at *ca.* 3200 mbsl rising *ca.* 500 m above the seafloor, which roughly coincides with the inferred position of the present hotspot.

The Challenger Fracture Zone, which is clear ∼100 km south of the Alejandro Selkirk cluster, converges to the JFR and crosses in a diffuse zone somewhere between Alpha and Beta guyots, and also disturbs the magnetic anomalies of the seafloor fabric even west of Alejandro Selkirk Island (**Figure 1**). A magnetic fabric associated with this fracture zone is oblique to the JFR and defines an intrusive/extrusive domain that disrupts the regular fabric of the sea floor (Rodrigo and Lara, 2014). This feature resumes as a ∼N60-65°E linear bathymetric feature north of the JFR, where it offsets the magnetic anomalies of the seafloor in a left-lateral sense.

Geochemical Features

Juan Fernández Ridge samples are from the upper section of seamounts and islands (i.e., not including basal parts of the
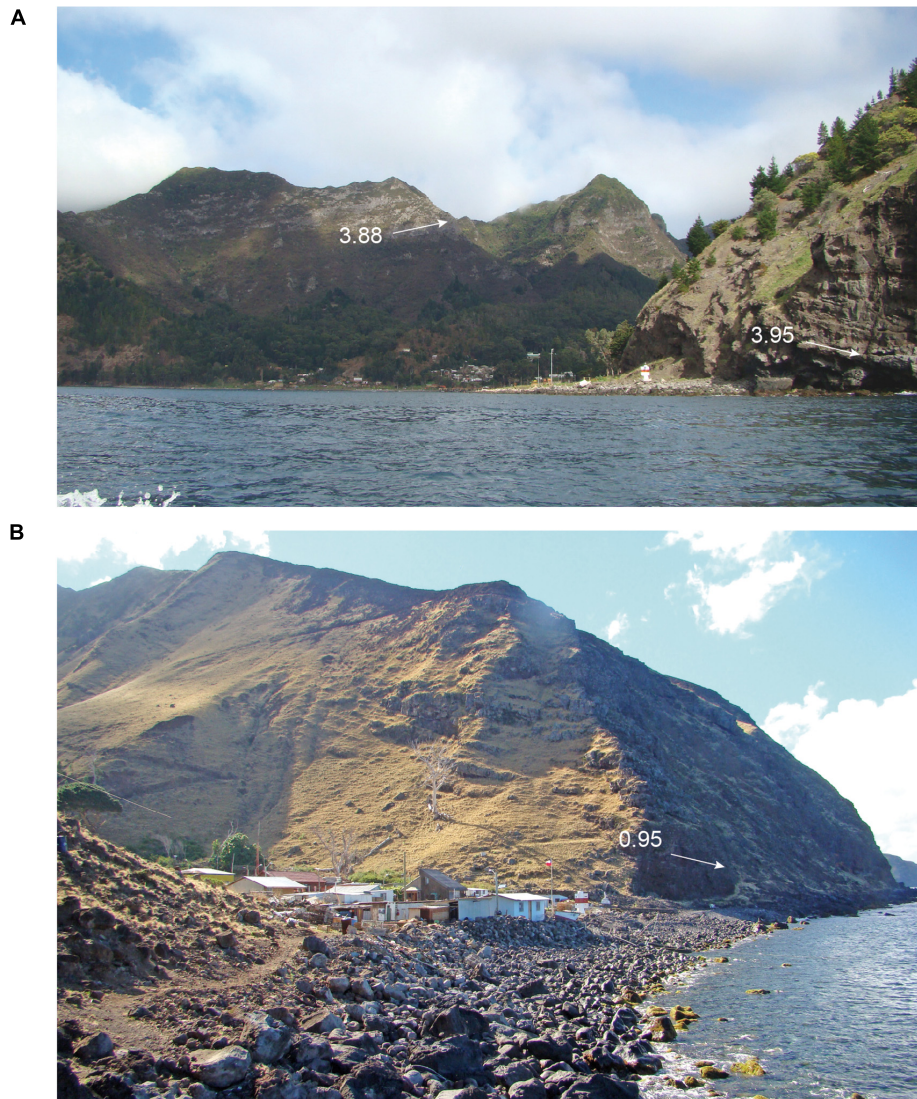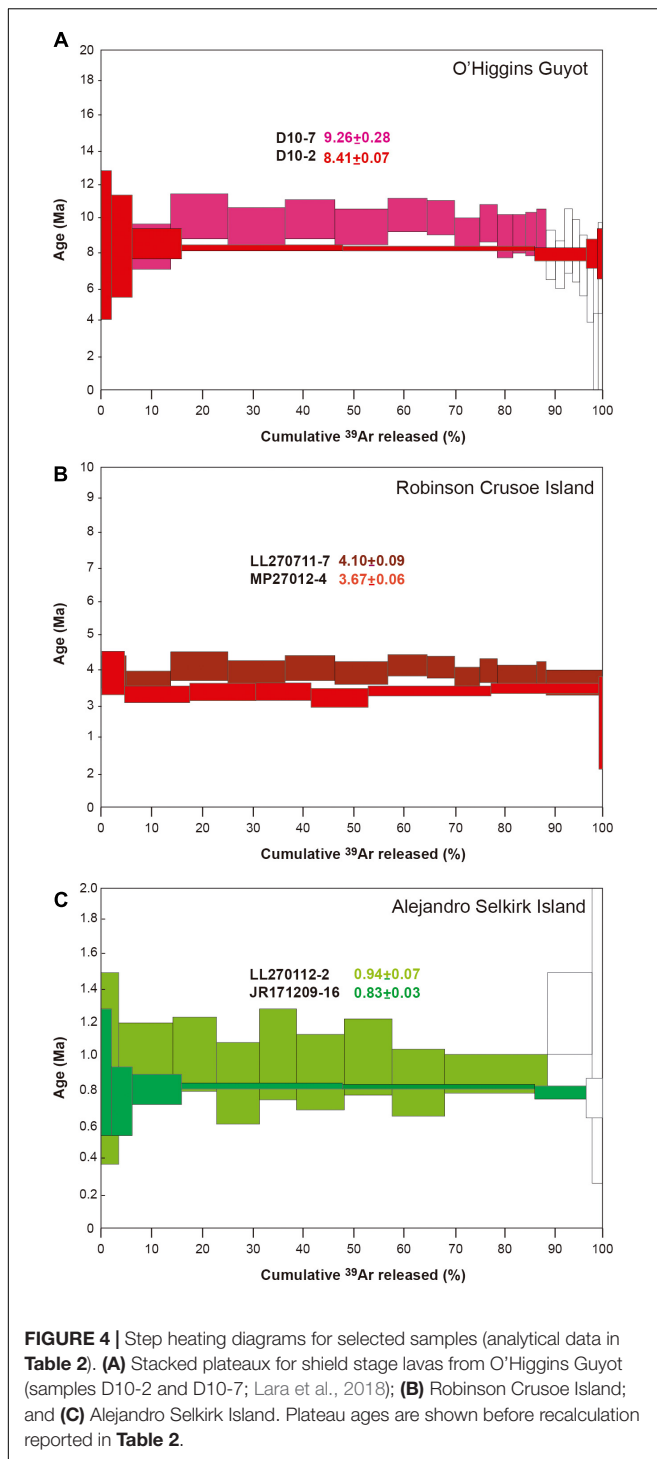
FIGURE 3 | Photographs representing the typical shield stage sequences of dominant tholeiitic basalts at Robinson Crusoe and Alejandro Selkirk islands.
(A) Panoramic view of Cumberland Bay and San Juan Bautista village, Robinson Crusoe Island, with the exposed *ca*. 900 m thick, NE gently dipping sequence.
(B) View of 'Quebrada de las Casas' village in Alejandro Selkirk Island and the exposed E dipping sequence. Numbers are $^{40}Ar/^{39}Ar$ ages (see **Table 2** for analytical details) in their stratigraphic position (white arrows).

major edifices) and rock types are mostly tholeiitic basalts and scarce alkaline basalts and basanites, representing both the shield and rejuvenated stages (**Figure 4**). As described from other hotspot volcanoes (e.g., Konter and Jackson, 2012; Garcia et al., 2016), basanites are typical of the rejuvenated stage, and they have been recovered from Robinson Crusoe Island (Reyes et al., 2017) and O'Higgins Guyot (Lara et al., 2018). We here focus on the shield stage, and because samples come from the upper slope of seamounts and from the subaerial sections of Alejandro Selkirk and Robinson Crusoe islands, they most likely represent the late shield stage. Summarizing the main geochemical features of the shield stage based on recent results (Reyes et al., 2017; Truong et al., 2018) and our ongoing research, JFR is formed by basic lavas highly

enriched in incompatible elements (LIL and HFSE) compared to MORB, probably due to a more enriched mantle source and smaller degrees of melting. This geochemical enrichment is more marked in Robinson Crusoe Island and Alpha Guyot, and extends to higher La/Sm and Nb/Zr ratios compared to O'Higgins Guyot and Alejandro Selkirk Island (**Figure 4**). These features could be explained by differences in the partial melting degree and mantle potential temperature, although subtle changes in the composition of the source over time could also be playing a role. Basanites are also present at Friday Seamount and lavas from Domingo carry some signatures that mimic those recognized in lavas from the rejuvenated stage in O'Higgins Guyot and Robinson Crusoe Island (Reyes et al., 2017; Lara et al., 2018). Devey et al. (2000) interpreted these

FIGURE 4 | Step heating diagrams for selected samples (analytical data in **Table 2**). **(A)** Stacked plateaux for shield stage lavas from O'Higgins Guyot (samples D10-2 and D10-7; Lara et al., 2018); **(B)** Robinson Crusoe Island; and **(C)** Alejandro Selkirk Island. Plateau ages are shown before recalculation reported in **Table 2**.
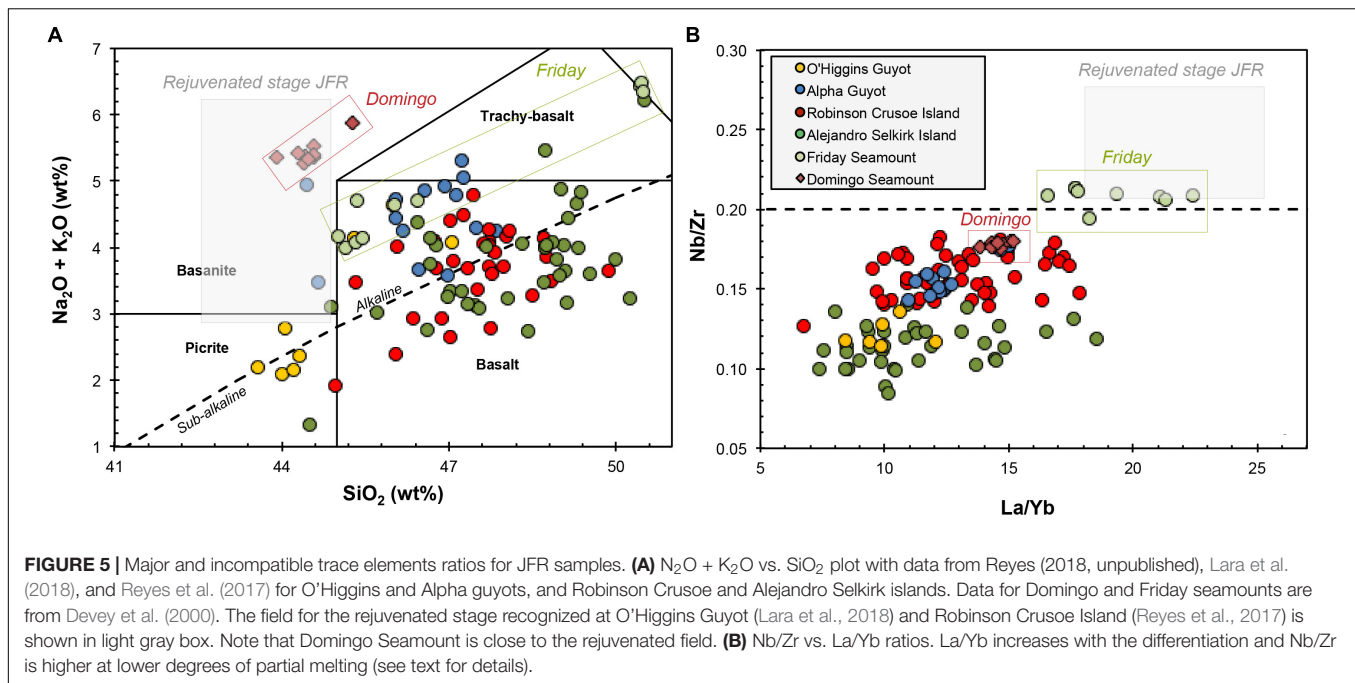
be explained only by changes in the degree of partial melting and thus subtle variations in the enriched source are needed. These mantle heterogeneities could also explain the low values of ^{3}He/^{4}He in Alejandro Selkirk compared to the higher values reported for Robinson Crusoe (Farley et al., 1993; Truong et al., 2018), the latter usually interpreted as evidence of an origin in the deep mantle (Hahm et al., 2009) and one of the most compelling probes of a mantle plume involvement in JFR. Despite the internal variation, the narrow field of isotopic values implies a relatively stable source beneath JFR, which is in contrast to the large variation observed in coeval chains on the Nazca Plate like the Easter Seamount Chain (Ray et al., 2012), where a mixture of enriched and depleted sources has been proposed (e.g., Kingsley and Schilling, 1998; Simons et al., 2002). Data from San Félix and San Ambrosio islands also reflect mantle heterogeneities beneath the Nazca Plate in the SE Pacific (Gerlach et al., 1986).

RESULTS

Ages and Age Progression

Seventeen new ^{40}Ar/^{39}Ar ages, and 3 recently published (Reyes et al., 2017; Lara et al., 2018) were determined from experiments that yield well defined plateaux following Sharp and Renne (2005), all comprising > 60% of the ^{39}Ar released, with probability of fits of at least 0.05, and having no resolvable slopes (**Figure 5** and **Table 2**). Isochron regressions (York, 1969) indicate that ^{40}Ar/^{36}Ar intercepts are indistinguishable from the atmospheric value of 295.5 (Steiger and Jagger, 1977). Thus, we consider the plateau ages as the best estimate of the time elapsed since eruption or cooling below closure temperature and we used these data to calculate the age progression and cumulative eruptive volumes. In two cases we preferred the isochrones because of the lower uncertainty at 2σ.

Radioisotopic ages form a linear array when plotted against great circle distance to Domingo Seamount (thought to be near the present hotspot) and thus a clear age progression. We obtain thus a velocity of 81.30 ± 1.70 mm/year ($R^2 = 0.96$) using all the samples, which is slightly better when only latest shield stage samples are considered (80.65 ± 1.70 mm/year with $R^2 = 0.99$) (**Figure 6**). There are no significant outliers, even taking into account the poorly constrained stratigraphic position for submarine samples. For example, Domingo and the more mature Friday Seamount are probably in the early stage of shield volcanism and thus only comparable with the unsampled, older section of the others. We included Friday Seamount age in the regression despite its signature comparable with that of the rejuvenated stage, basically because of the short time span represented by these lavas. In fact, when the age of Friday Seamount is excluded, the trendline does not change significantly. On the other hand, the regression line predicts younger ages for Robinson Crusoe Island, which is expected since all the samples are from the exposed stratigraphic section with an eroded section of yet unknown thickness inferred. From the reported ages in consecutive seamounts along the JFR, the duration of the shield stage would have been *ca.* 1 My. From

features as the effect of source metasomatism at early stages of extrusion.

Published Sr-Nd-Pb isotopic ratios suggest source enrichment with respect to depleted mantle source of MORB (Farley et al., 1993; Truong et al., 2018), including those from the East Pacific Rise and North Chile Ridge and excluding the extensive participation of the lithospheric mantle. Local differences cannot

FIGURE 5 | Major and incompatible trace elements ratios for JFR samples. **(A)** $N_2O + K_2O$ vs. SiO_2 plot with data from Reyes (2018, unpublished), Lara et al. (2018), and Reyes et al. (2017) for O'Higgins and Alpha guyots, and Robinson Crusoe and Alejandro Selkirk islands. Data for Domingo and Friday seamounts are from Devey et al. (2000). The field for the rejuvenated stage recognized at O'Higgins Guyot (Lara et al., 2018) and Robinson Crusoe Island (Reyes et al., 2017) is shown in light gray box. Note that Domingo Seamount is close to the rejuvenated field. **(B)** Nb/Zr vs. La/Yb ratios. La/Yb increases with the differentiation and Nb/Zr is higher at lower degrees of partial melting (see text for details).

the regression line, the intercept at $y = 0$ implies that the hotspot is presently *ca.* 20 km west of the Domingo Seamount (33°55.5′S/82°2.9′W).

Volumes and Eruptive Rates

We use radiometric ages obtained for shield units and independently estimated volumes from bathymetry to document changes in the eruptive volumes over time (**Figure 7**). We found that the 400 km gap between O'Higgins seamounts and the western JFR segment marks a temporal gap of *ca.* 4 Ma without eruptive record. The onset of a period with the highest eruptive rate occurred at 5.5 Ma and lasted for *ca.* 2 My (from Gamma to Robinson Crusoe). A more moderate growth period extended from *ca.* 3–1.5 Ma (Duke to Alejandro Selkirk) and the more recent episode occurred at an even lower eruption rate. The earlier low volumetric growth period coincides with a decreasing difference between the age of the oceanic crust and the age of volcanism (Δ_{age} in **Figure 7**); the rapid growth period occurs with a nearly constant Δ_{age} and the change to a lower growth rate is accompanied by a slight increase in Δ_{age}, which also corresponds to the intersection of the Challenger Fracture Zone (**Figure 7**). On the other hand, geochemical tracers only show minor changes along the chain (related to variations in partial melting degree and subtle mantle source changes) and thus volumes, eruptive rates and continuity of the alignment seems to be independent of the nature of the source.

DISCUSSION

Velocity of the Nazca Plate

Age progressions along hotspot trails are useful to test absolute plate tectonic models. The early idea of a possible age progression

along JFR was based on very few imprecise K-Ar dates for Robinson Crusoe and Alejandro Selkirk islands and a single total fusion $^{40}Ar/^{39}Ar$ date for the O'Higgins Guyot. Despite the high uncertainty of these values, the velocity inferred for the Nazca Plate is not significantly different from our result, which is based on more precise radiometric dating. The velocity here obtained is close to the value deduced at Domingo Seamount with the NUVEL 1A model (DeMets et al., 1994) and slightly higher than that obtained with MORVEL (DeMets et al., 2010). However, these models are in a no-net-rotation frame, and when converted to fixed-hotspot frames, inferred velocities are much lower. When absolute plate models with moving hotspots are considered (e.g., T25M by Wang et al., 2018; 57.04 mm/year at Domingo Seamount), the difference is less and could be reconciled with a *ca.* 20 mm/year westward drift of the mantle plume. In addition, if the convergence rate between the Nazca and South-American plates is higher than the inferred absolute motion of the Nazca Plate, then South America is advancing toward the trench. In fact, Schepers et al. (2017) showed that South-American Plate advance has been accompanied by > 200 km of trench retreat since ∼12 Ma.

On the other hand, our estimated velocity for the Nazca Plate is lower than the value published by Ray et al. (2012) based on the age progression along the coeval Easter Seamount Chain (110 mm/year for the range 0–20 Ma). In order to perform a more robust comparison, we scrutinized the dates obtained by Ray et al. (2012) removing values possibly related to rejuvenated stages (those with Nb/Zr > 0.2 and La/Yb > 15 being also clear age outliers) and those without clear plateau ages. For this subset we obtained a slightly lower velocity of 106.38 mm/year ($R^2 = 0.96$) when all the < 20 Ma samples are taken into account. A closer inspection in this range allow us to identify a break at *ca.* 10 Ma from which we obtain a velocity of 89.29 mm/year ($R^2 = 0.99$)
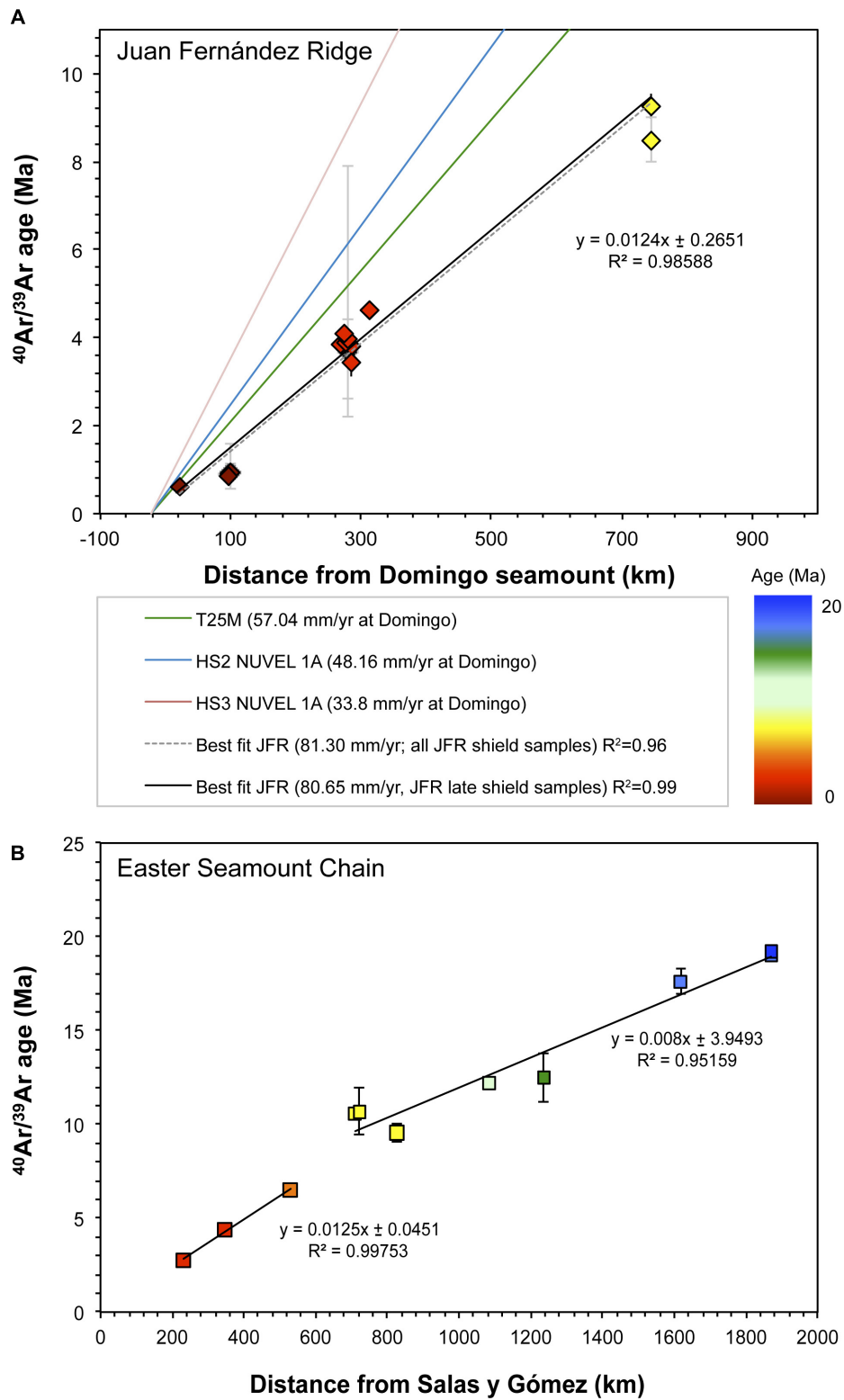
FIGURE 6 | ^{40}Ar/^{39}Ar groundmass age vs. great circle distance from Domingo Seamount **(A)**. A linear regression line is shown with corresponding equation and coefficient of determination R^2. Lower panel in **(B)** shows the correlation for Easter Seamount Chain (data modified from Ray et al., 2012 only removing the outliers in the range 0–10 Ma). Velocity from the T25M model taking into account moving hotspots (Wang et al., 2018) is shown for comparison, together with other fixed hotspots plate tectonic models as NUVEL 1A (DeMets et al., 1994) and MORVEL56 (DeMets et al., 2010) computed at Domingo Seamount.
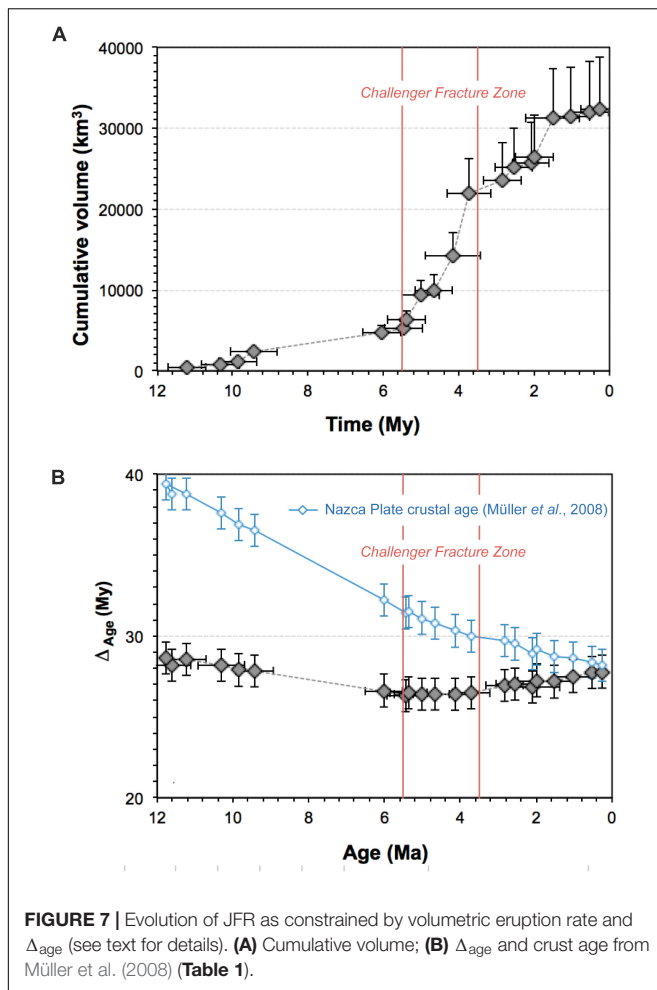
FIGURE 7 | Evolution of JFR as constrained by volumetric eruption rate and Δ_{age} (see text for details). **(A)** Cumulative volume; **(B)** Δ_{age} and crust age from Müller et al. (2008) (**Table 1**).

for samples < 10 Ma (**Figure 7**). Despite the uncertainty of radiometric dating, this value is closer to the velocity deduced from the JFR and thus both seems to unravel coherent drift of mantle plumes beneath the Nazca Plate.

A Weak Primary Mantle Plume Beneath JFR?

Preliminary geochemical evidence suggests the possible involvement of pyroxenite in the source of JFR magmas. Our modeling effort (e.g., Reyes, 2018, unpublished) shows in fact a spatially heterogeneous mantle plume beneath JFR with a minor but relevant pyroxenite fraction (5–12%) and a relatively low potential temperature (T_p, ca. 1330°C). This model T_p is low, in general, compared to some other OIB (e.g., Herzberg et al., 2007; Putirka, 2008; Kimura and Kawabata, 2015), but similar or slightly higher than some estimates for the ambient mantle temperature, e.g., ~1396°C (Putirka, 2008), ~1280–1400°C (Herzberg et al., 2007) or ~1300–1310°C (Kimura and Kawabata, 2015), the latter calculated with the same method. A low temperature in a pyroxenite-bearing plume could be explained by its disposition to cool because of the low ascent velocity imparted by its density, high viscosity (Adam et al.,

2017) and its possible volatile content (e.g., Devey et al., 2000). Thus, although a more precise appraisal of the nature of the mantle plume beneath JFR is beyond the scope of this article, we speculate that discontinuities along the JFR, and the variations of the eruptive rates, could be a result of the weakness of the feeding mantle plume with temporal changes in T_p implying different partial melting degree over time.

In addition, gaps and changes in volumetric magma production could be also related to the dynamic nature of the oceanic plate. Orellana-Rovirosa and Richards (2017) proposed a dimensionless parameter (R) as a proxy for rough or smooth topography along seamount chains, with $R < 1.5$ for rough, discontinuous ridges and $R > 3$ for those with a smooth topography. R is approximated by the equation $R = (Q/V)^{-2}/T_e$ as function of buoyancy flux Q (m^3/s), plate velocity V (m/s) and elastic thickness of the lithosphere T_e (m). When computing R for JFR with appropriate values (buoyancy flux = 0.19 m^3/s from the review by King and Adam, 2014; T_e = 5–15 km from Manríquez et al., 2013) we obtain 1.3 ± 0.5, which is consistent with a mostly rough topography. From that reasoning we speculate that a low buoyancy flux combined with an old oceanic lithosphere (ca. 26 Ma at the time of volcanism) are the main controlling factors for the observed discontinuity. A low buoyancy flux is also consistent with a low volumetric eruption rate (**Figure 7**), and also with an independently estimated low T_p in the pyroxenite-bearing source. Recent global seismic tomography (French and Romanowicz, 2015) beneath JFR shows a partially resolved anomaly of low shear-wave velocities that is consistent with this interpretation.

A Reappraisal of the JFR Collision Against the Continental Margin Over Time

The apparent age progression along JFR was used by a number of authors to assess the possible geological effects of the collision of this ridge against the continental margin (e.g., Martinod et al., 2010 and references therein). Some of them proposed a fast migration velocity of the collision point (Yáñez et al., 2001) based on an extremely sharp ridge bending at ca. 25–26 Ma (from ENE to NNE). However, close inspection of the intraslab seismicity reported by Kirby et al. (1996), and the updated picture by Clouard et al. (2007) from the NEIC catalog (1993–2003), shows a clear pattern of earthquakes clustering in an ENE trend (N78°E), which coincides with the convergence vector, and the absence of any major bending of the seismicity at depth that shed light on the older JFR segment. In addition, the geometry of the Easter Seamount Chain shows a more complex pattern instead of a simple bending when it continues on the Nazca Ridge at ca. 25 Ma. The latter is a NE-trending structure and could be a closer analog of the subducted portion of the JFR older than 25 Ma. Thus, we consider NE rather than NNE as a more plausible trend for the older Oligocene segment and hence a lower migration velocity of the collision point would be implied. A recent study of the ridge-trench collision along the Andean margin by Bello-González et al. (2018) reaches the same conclusion based on a reconstruction of the Nazca Plate hotspot trails.

On the other hand, and more directly related to the younger segment of the JFR, we interpret the morphology and alignment of the O'Higgins seamounts as indicating a more recent and gradual change in the strike of the JFR that would produce a gentle concavity to the north ($\sim$15–20°). This hypothesis was also considered by von Huene et al. (1997), but discarded because of apparent inconsistency with other temporal and physical indicators. One objection came from the apparent absence of an equivalent geometry in the coeval segment of the Easter Seamount Chain. Interestingly, and despite the rough morphological continuity, the Easter Seamount Chain does show a jump in the age progression just at *ca.* 9–10 Ma after removal of the anomalous values reported by Ray et al. (2012) (**Figure 6**). There is not a clear reason for such a subtle bending because the Nazca Plate has been stable after the last major reorganization at 26 Ma (Tebbens and Cande, 1997), although changes in the Nazca-South America convergence velocity have been reported (e.g., *ca.* 5% reduction of convergence velocity at 10 Ma and 20% at 5 Ma; Somoza and Ghidella, 2012). Most importantly, Tebbens et al. (1997) found an increase of the half spreading rate at the Chile Ridge at $\sim$9.58 Ma (from 37.8 to 45.6 mm/year), which could be enough to drive some change in the plate movement considering that the south portion of the Nazca Plate is being created at the Chile Ridge. Thus, we suggest that the JFR trace has a primary curvature with an inflection point at O'Higgins seamounts, now accentuated by the NE-trending structural fabric acquired in the outer-rise region.

Taking advantage of refined plate tectonic models (e.g., Seton et al., 2012) and tools in GPlates 2.0 (Cannon et al., 2014), we used the rectified JFR trace to reconstruct the migration of the collision point over time (with South-American Plate fixed and JFR parallel to the convergence velocity). Our preliminary result yields a velocity of *ca.* 90 ($\pm$ 20) mm/year southward from 15 to 10 Ma, which is lower than the value of *ca.* 200 mm/year obtained by Yáñez et al. (2001) and comparable with the value reported by Bello-González et al. (2018). For this reconstruction we partially modified the subducted segment older than 25 Ma to be parallel to the Nazca Ridge, a reasonable assumption before the major plate reorganization at *ca.* 26 Ma. If a restored continental margin is considered as in Arriagada et al. (2008, 2013) and Martinod et al. (2010), an even lower value would be obtained. Despite the significant uncertainty, the latter imply that JFR arrived at 27–28°S (northern limit of the Pampean flat slab segment) at *ca.* 15 Ma, and reached 31°S at *ca.* 10 Ma migrating since then at a lower velocity (*ca.* 25 mm/year). This slower migration velocity seems to be more consistent with the gradual initiation of the flat slab at this latitude (e.g., Kay et al., 1991), where the arc front started to decline in the Upper Miocene but persisted until Late Pliocene (Bissig et al., 2002), and the evidence of protracted uplift at coastal areas (e.g., Le Roux et al., 2005).

CONCLUSION

Juan Fernández Ridge is a *ca.* 800 km long and partially discontinuous chain of seamounts and islands in the Nazca Plate. 17 new and 3 recently published ^{40}Ar/^{39}Ar ages

indicate a clear age progression with a mean velocity of *ca.* 81 mm/year. This is consistent with an origin of the JFR above a hotspot rooted in a mantle plume. The inferred velocity is much higher than obtained from models based on stationary hotspots, and still higher than those absolute plate motion models that consider moving mantle plumes. A westward drift of the mantle plume beneath JFR is thus implied. Morphological discontinuity along the ridge and along chain variations of the eruptive rates could be either related to changes in the petrological signature of the source and/or the dynamic nature of the overriding plate. Preliminary geochemical evidence suggests the possible involvement of a pyroxenite-bearing source from which low temperatures and low ascent velocities could be inferred. Such a nature of the source and the overlying lithosphere could explain both the diffuse geophysical signature of the plume and its intermittent upwelling. Both the age progression along the JFR based on new geocronological data and a detailed inspection of the morphology at O'Higgins seamounts cluster, allow a reappraisal of the subducted segment and hence a review of some of the postulated effects of the collision against the continental margin, at least during the last 15 Ma.

REFERENCES

Adam, C., Caddick, M. J., and King, S. D. (2017). Pyroxenite causes fat plumes and stagnant slabs. *Geophys. Res. Lett.* 44, 4730–4737. doi: 10.1002/2017GL072943

Amante, C., and Eakins, B. W. (2009). *ETOPO1 1 Arc-Minute Global Relief Model: Procedures, Data Sources and Analysis. NOAA Technical Memorandum NESDIS NGDC-*24. Silver Spring, MD: NOAA, doi: 10.7289/V5C8276M

Anderson, D. (2005). "Scoring hotspots: the plume and plate paradigms," in *Plates, Plumes, and Paradigms: Geological Society of America Special Paper 388*, eds G. R. Foulger, J. H. Natland, D. C. Presnall, and D. L. Anderson (Boulder, CO: Geological Society of America), 31–54. doi: 10.1130/0-8137-2388-4.31

Argus, D. F., Gordon, R. G., Heflin, M. B., Ma, C., Eanes, R. J., Willis, P., et al. (2010). The angular velocities of the plates and the velocity of Earth's centre from space geodesy. *Geophys. J. Int.* 180, 913–960. doi: 10.1111/j.1365-246X.2009.04463.x

Arriagada, C., Ferrando, R., Córdova, L., Morata, D., and Roperch, P. (2013). The Maipo Oroclinе: a first scale structural feature in the Miocene to Recent geodynamic evolution in the central Chilean Andes. *Andean Geol.* 40, 419–437. doi: 10.5027/andgeoV40n3-a02

Arriagada, C., Roperch, P., Mpodozis, C., and Cobbold, P. R. (2008). Paleogene building of the Bolivian Orocline: tectonic restoration of the Central Andes in 2-D map view. *Tectonics* 27:TC6014. doi: 10.1029/2008TC002269

Astudillo, V. (2014). *Geomorfología y Evolución Geológica de la isla Robinson Crusoe, Archipiélago Juan Fernández.* Ph.D. thesis Santiago, Universidad de Chile, 154.

Baker, P. E., Gledhill, A., Harvey, P. K., and Hawkesworth, C. J. (1987). Geochemical evolution of the Juan Fernández Islands, SE Pacific. *J. Geol. Soc. Lond.* 144, 933–944. doi: 10.1144/gsjgs.144.6.0933

Ballmer, M. D., van Hunen, J., Ito, G., Tackley, P. J., and Bianco, T. (2007). Non-hotspot volcano chains originating from small-scale sublithospheric convection. *Geophys. Res. Lett.* 34:L23310. doi: 10.1029/2007GL031636

Bello-González, J. P., Contreras-Reyes, E., and Arriagada, C. (2018). Predicted path for hotspot tracks off South America since Paleocene times: tectonic implications of ridge-trench collision along the Andean margin. *Gondwana Res.* 64, 216–234. doi: 10.1016/j.gr.2018.07.008

Bissig, T., Clark, A. H., and Lee, J. K. (2002). Cerro de Vidrio rhyolitic dome: evidence for Late Pliocene volcanism in the central Andean flat-slab region, Lama-Veladero district, 29° 20' S, San Juan Province, Argentina. *J. South Am. Earth Sci.* 15, 571–576. doi: 10.1016/S0895-9811(02)00077-9

Bonatti, E., Harrison, C. G. A., Fisher, D. E., Honnorez, J., Schilling, J. G., Stipp, J. J., et al. (1977). Easter volcanic chain (Southeast Pacific): a mantle hot line. *J. Geophys. Res.* 82, 2457–2478. doi: 10.1029/JB082i017p02457

Booker, J., Bullard, E. C., and Grasty, R. L. (1967). Palaeomagnetism and age of rocks from easter island and juan fernández. *Geophys. J. Int.* 12, 469–471. doi: 10.1111/j.1365-246X.1967.tb03127.x

Cande, S. C., and Haxby, W. F. (1991). Eocene propagating rifts in the southwest Pacific and their conjugate features on the Nazca Plate. *J. Geophys. Res.* 96, 148–227. doi: 10.1029/91JB01991

Cannon, J., Lau, E., and Müller, R. D. (2014). Plate tectonic raster reconstruction in GPlates. *Solid Earth Dis.* 5, 741–755. doi: 10.5194/se-5-741-2014

Caress, D. W., and Chayes, D. N. (2017). *MB-System: Mapping the Seafloor.* Available at: https://www.mbari.org/products/research-software/mb-system

Clouard, V., and Bonneville, A. (2001). How many Pacific hotspots are fed by deep-mantle plumes? *Geology* 29, 695–698. doi: 10.1130/0091-7613(2001)029<0695:HMPHAF>2.0.CO;2

Clouard, V., Campos, J., Lemoine, A., Perez, A., and Kausel, E. (2007). Outer rise stress changes related to the subduction of the Juan Fernández Ridge, central Chile. *J. Geophys. Res.* 112:B05305. doi: 10.1029/2005JB003999

DeMets, C., Gordon, R. G., and Argus, D. F. (2010). Geologically current plate motions. *Geophys. J. Int.* 181, 1–80. doi: 10.1111/j.1365-246X.2009.04491.x

DeMets, C., Gordon, R. G., Argus, D. F., and Stein, S. (1994). Effect of recent revisions to the geomagnetic reversal time scale on estimates of current plate motions. *Geophys. Res. Lett.* 21, 2191–2194. doi: 10.1029/94GL02118

Devey, C. W., Hémond, C., and Stoffers, P. (2000). Metasomatic reactions between carbonated plume melts and mantle harzburgite: the evidence from Friday and Domingo Seamounts (Juan Fernández chain, SE Pacific). *Contrib. Mineral. Petrol.* 139, 68–84. doi: 10.1007/s004100050574

Farley, K. A., Basu, A. R., and Craig, H. (1993). He, Sr and Nd isotopic variations in lavas from the Juan Fernández archipelago, SE pacific. *Contrib. Mineral. Petrol.* 115, 75–87. doi: 10.1007/BF00712980

Fleck, R. J., Sutter, J. F., and Elliot, D. H. (1977). Interpretation of discordant 40Ar/39Ar age-spectra of Mesozoic tholeiites from Antarctica. *Geochim. Cosmochim. Acta* 41, 15–32. doi: 10.1016/0016-7037(77)90184-3

Flueh, E. R., Kopp, H., and Schreckenberger, B. (2002). *SPOC (SONNE Cruise SO-161 Leg 1 and 4), Subduction Processes off Chile, Geomar Rep. 102.* Kiel: Geomar.

French, S. W., and Romanowicz, B. (2015). Broad plumes rooted at the base of the Earth's mantle beneath major hotspots. *Nature* 525, 95–99. doi: 10.1038/nature14876

Garcia, M. O., Weis, D., Jicha, B. R., Ito, G., and Hanano, D. (2016). Petrology and geochronology of lavas from Ka'ula Volcano: implications for rejuvenated volcanism of the Hawaiian mantle plume. *Geochim. Cosmochim. Acta* 185, 278–301. doi: 10.1016/j.gca.2016.03.025

Gerlach, D. C., Hart, S. R., Morales, V. W. J., and Palacios, C. (1986). Mantle heterogeneity beneath the Nazca plate: san Felix and Juan Fernández islands. *Nature* 322, 165–169. doi: 10.1038/322165a0

Hahm, D., Castillo, P., and Hilton, D. (2009). A deep mantle source for high 3He/4He ocean island basalts (OIB) inferred from Pacific near-ridge seamount lavas. *Geophys. Res. Lett.* 36:L20316. doi: 10.1029/2009GL040560

Herzberg, C., Asimow, P. D., Arndt, N., Niu, Y., Lesher, C. M., Fitton, J. G., et al. (2007). Temperatures in ambient mantle and plumes: constraints from basalts, picrites, and komatiites. *Geochem. Geophys. Geosyst.* 8, 1–34. doi: 10.1029/2006GC001390

Hirano, N., Machida, S., Abe, N., Morishita, T., Tamura, A., and Arai, S. (2013). Petit-spot lava fields off the central Chile trench induced by plate flexure. *Geochem. J.* 47, 249–257. doi: 10.2343/geochemj.2.0227

Hirano, N., Takahashi, E., Yamamoto, J., Abe, N., Ingle, S. P., Kaneoka, I., et al. (2006). Volcanism in response to plate flexure. *Science* 313, 1426–1428. doi: 10.1126/science.1128235

Jackson, M. G., Konter, J. G., and Becker, T. W. (2017). Primordial helium entrained by the hottest mantle plumes. *Nature* 542, 340–343. doi: 10.1038/nature21023

Jicha, B. R., and Brown, F. H. (2014). An age for the Korath Range, Ethiopia and the viability of 40Ar/39Ar dating of kaersutite in Late Pleistocene volcanics. *Quat. Geochronol.* 21, 53–57. doi: 10.1016/j.quageo.2013.03.007

Jicha, B. R., Singer, B. S., and Sobol, P. (2016). Re-evaluation of the ages of 40Ar/39Ar sanidine standards and supereruptions in the western US using a Noblesse multi-collector mass spectrometer. *Chem. Geol.* 431, 54–66. doi: 10.1016/j.chemgeo.2016.03.024

Kay, S. M., Mpodozis, C., Ramos, V. A., and Munizaga, F. (1991). Magma source variations for mid-late Tertiary magmatic rocks associated with a shallowing subduction zone and the thickening crust in the central Andes (28-33°S). *Spec. Pap. Geol. Soc. Am.* 265, 113–137. doi: 10.1130/SPE265-p113

Kimura, J. I., and Kawabata, H. (2015). Ocean Basalt Simulator version 1 (OBS1): trace element mass balance in adiabatic melting of a pyroxenite-bearing peridotite. *Geochem. Geophys. Geosyst.* 16, 267–300. doi: 10.1002/2014GC005606

King, S. D., and Adam, C. (2014). Hotspot swells revisited. *Phys. Earth Planet. Inter.* 235, 66–83. doi: 10.1016/j.pepi.2014.07.006

Kingsley, R. H., and Schilling, J. G. (1998). Plume-ridge interaction in the Easter-Salas y Gomez seamount chain-Easter Microplate system: Pb isotope evidence. *J. Geophys. Res. Solid Earth* 103, 24159–24177. doi: 10.1029/98JB01496

Kirby, S., Engdahl, R. E., and Denlinger, R. (1996). Intermediate-depth intraslab earthquakes and arc volcanism as physical expressions of crustal and uppermost mantle metamorphism in subducting slabs. *Geophys. Monogr. Ser.* 96, 195–214. doi: 10.1029/GM096p0195

Konter, J. G., and Jackson, M. G. (2012). Large volumes of rejuvenated volcanism in Samoa: evidence supporting a tectonic influence on late-stage volcanism. *Geochem. Geophys. Geosyst.* 13:Q0AM04. doi: 10.1029/2011GC003974

Kopp, H., Flueh, E. R., Papenberg, C., and Klaeschen, D. (2004). Seismic investigations of the O'Higgins Seamount Group and Juan Fernández Ridge: aseismic ridge emplacement and lithosphere hydration. *Tectonics* 23:TC2009. doi: 10.1029/2003TC001590

Kuiper, K. F., Deino, A., Hilgen, F. J., Krijgsman, W., Renne, P. R., and Wijbrans, J. R. (2008). Synchronizing rock clocks of earth history. *Science* 320, 500–504. doi: 10.1126/science.1154339

Lara, L. E., Díaz-Naveas, J., Reyes, J., Jicha, B., Orozco, G., and Kay, S. M. (2018). Unraveling short-lived rejuvenated volcanism and a rapid transition from shield stage at O'Higgins Guyot, Juan Fernández Ridge, Pacific SE. *Deep Sea Res. Part I Oceanogr. Res. Pap.* 141, 33–42. doi: 10.1016/j.dsr.2018.08.012

Lara, L. E., Moreno, H., Naranjo, J. A., Matthews, S., and Pérez de Arce, C. (2006). Magmatic evolution of the Puyehue-Cordón Caulle Volcanic Complex (40°S), Southern Andean Volcanic Zone: from shield to unusual rhyolitic fissure volcanism. *J. Volcanol. Geotherm. Res.* 157, 343–366. doi: 10.1016/j.jvolgeores.2006.04.010

Laursen, J., and Normark, W. R. (2002). Late Quaternary evolution of the San Antonio Submarine Canyon in the central Chile forearc (33°S). *Mar. Geol.* 188, 365–390. doi: 10.1016/S0025-3227(02)00421-8

Laursen, J., Scholl, D. W., and von Huene, R. (2002). Neotectonic deformation of the central Chile margin: deepwater forearc basin formation in response to hot spot ridge and seamount subduction. *Tectonics* 21, 2-1–2-27. doi: 10.1029/2001TC901023

Le Roux, J. P., Gómez, C. A., Olivares, D. M., and Middleton, H. (2005). Determining the Neogene behavior of the Nazca plate by geohistory analysis. *Geology* 33, 165–168. doi: 10.1130/G21101.1

Manríquez, P., Contreras-Reyes, E., and Osses, A. (2013). Lithospheric 3-D flexure modelling of the oceanic plate seaward of the trench using variable elastic thickness. *Geophys. J. Int.* 196, 681–693. doi: 10.1093/gji/ggt464

Martinod, J., Husson, L., Roperch, P., Guillaume, B., and Espurt, N. (2010). Horizontal subduction zones, convergence velocity and the building of the Andes. *Earth Planet. Sci. Lett.* 300, 299–309. doi: 10.1016/j.epsl.2010.09.010

McDougall, I. (1964). Potassium-argon ages from lavas of the Hawaiian Islands. *Geol. Soc. Am. Bull.* 75, 107–128. doi: 10.1130/0016-7606(1964)75[107:PAFLOT]2.0.CO;2

McDougall, I. (1971). Volcanic island chains and sea floor spreading. *Nature* 231, 141–144. doi: 10.1038/physci231141a0

Mercer, C. M., and Hodges, K. V. (2016). ArAR-A software tool to promote the robust comparison of K-Ar and 40Ar/39Ar dates published using different decay, isotopic, and monitor-age parameters. *Chem. Geol.* 440, 148–163. doi: 10.1016/j.chemgeo.2016.06.020

Min, K., Mundil, R., Renne, P. R., and Ludwig, K. R. (2000). A test for systematic errors in 40Ar/39Ar geochronology through comparison with U/Pb analysis of a 1.1-Ga rhyolite. *Geochim. Cosmochim. Acta* 64, 73–98. doi: 10.1016/S0016-7037(99)00204-5

Mitchell, N. C. (2001). Transition from circular to stellate forms of submarine volcanoes. *J. Geophys. Res. Solid Earth* 106, 1987–2003. doi: 10.1029/2000JB900263

Morgan, W. J. (1971). Convection plumes in the lower mantle. *Nature* 230, 42–43. doi: 10.1038/230042a0

Morgan, W. J. (1972). Deep mantle convection plumes and plate motions. *Am. Assoc. Pet. Geol. Bull.* 56, 203–213. doi: 10.1038/nature17422

Müller, R. D., Sdrolias, M., Gaina, C., and Roest, W. R. (2008). Age, spreading rates, and spreading asymmetry of the world's ocean crust. *Geochem. Geophys. Geosyst.* 9:Q04006. doi: 10.1029/2007GC001743

Orellana-Rovirosa, F., and Richards, M. (2017). Rough versus smooth topography along oceanic hotspot tracks: observations and scaling analysis. *Geophys. Res. Lett.* 44, 4074–4081. doi: 10.1002/2016GL072008

Putirka, K. (2008). Excess temperatures at ocean islands: implications for mantle layering and convection. *Geology* 36, 283–286. doi: 10.1130/G24615A.1

Ramos, V., Cristallini, E. O., and Pérez, D. J. (2002). The Pampean flat-slab of the Central Andes. *J. South Am. Earth Sci.* 15, 59–78. doi: 10.1016/S0895-9811(02)00006-8

Ramos, V., and Folguera, A. (2009). Andean flat-slab subduction through time. *Geol. Soc. Lond. Spec. Publ.* 327, 31–54. doi: 10.1144/SP327.3

Ranero, C. R., von Huene, R., Weinrebe, W., and Reichert, C. (2006). "Tectonic processes along the Chile convergent margin," in *The Andes-Active Subduction Orogeny*, eds O. Oncken, G. Chong, G. Franz, P. Giese, H.-J. Götze, V. Ramos, et al. (Berlin: Springer), 91–121. doi: 10.1007/978-3-540-48684-8_5

Ray, J. S., Mahoney, J. J., Duncan, R. A., Ray, J., Wessel, P., and Naar, D. F. (2012). Chronology and geochemistry of lavas from the Nazca Ridge and Easter Seamount Chain: a 30 Myr hotspot record. *J. Petrol.* 53, 1417–1448. doi: 10.1093/petrology/egs021

Reich, M., Parada, M. A., Palacios, C., Dietrich, A., Schultz, F., and Lehmann, B. (2003). Adakite-like signature of Late Miocene intrusions at the Los Pelambres giant porphyry copper deposit in the Andes of central Chile: metallogenic implications. *Miner. Depos* 38, 876–885. doi: 10.1007/s00126-003-0369-9

Reichert, C., and Schreckenberger, B. (2002). Cruise Report SO161, leg 2&3, SPOC, subduction processes off Chile. *BGR Int. Rep.* 1–154.

Renne, P. R., Deino, A. L., Walter, R. C., Turrin, B. D., Swisher, C. C., Becker, T. A., et al. (1994). Intercalibration of astronomical and radioisotopic time. *Geology* 22, 783–786. doi: 10.1130/0091-7613(1994)022<0783:IOAART>2.3.CO;2

Reyes, J., Lara, L. E., and Morata, D. (2017). Contrasting P-T paths of shield and rejuvenated volcanism at Robinson Crusoe Island, Juan Fernández Ridge, SE Pacific. *J. Volcanol. Geotherm. Res.* 341, 242–254. doi: 10.1016/j.jvolgeores.2017.05.035

Rodrigo, C., and Lara, L. E. (2014). Plate tectonics and the origin of the Juan Fernández Ridge: analysis of bathymetry and magnetic patterns. *Lat. Am. J. Aquat. Res.* 42, 907–917. doi: 10.3856/vol42-issue4-fulltext-15

Rosenbaum, G., and Mo, W. (2011). Tectonic and magmatic responses to the subduction of high bathymetric relief. *Gondwana Res.* 19, 571–582. doi: 10.1016/j.gr.2010.10.007

Sandwell, D., and Fialko, Y. (2004). Warping and cracking of the Pacific plate by thermal contraction. *J. Geophys. Res.* 109:B10411. doi: 10.1029/2004JB003091

Schepers, G., Van Hinsbergen, D. J., Spakman, W., Kosters, M. E., Boschman, L. M., and McQuarrie, N. (2017). South-American plate advance and forced Andean trench retreat as drivers for transient flat subduction episodes. *Nat. Commun.* 8:15249. doi: 10.1038/ncomms15249

Sepúlveda, P., Le Roux, J. P., Lara, L. E., Orozco, G., and Astudillo, V. (2015). Biostratigraphic evidence for dramatic Holocene uplift of Robinson Crusoe Island, Juan Fernández Ridge, SE Pacific Ocean. *Biogeosciences* 12, 1993–2001. doi: 10.5194/bg-12-1993-2015

Seton, M., Müller, R. D., Zahirovic, S., Gaina, C., Torsvik, T., Shephard, G., et al. (2012). Global continental and ocean basin reconstructions since 200 Ma. *Earth Sci. Rev.* 113, 212–270. doi: 10.1016/j.earscirev.2012.03.002

Sharp, W. D., and Renne, P. R. (2005). The 40Ar/39Ar dating of core recovered by the Hawaii Scientific Drilling Project (phase 2), Hilo, Hawaii. *Geochem. Geophys. Geosyst.* 6:18. doi: 10.1029/2004GC000846

Simons, K., Dixon, J., Schilling, J.-G., Kingsley, R., and Poreda, R. (2002). Volatiles in basaltic glasses from the Easter-Salas y Gomez Seamount Chain and Easter Microplate: implications for geochemical cycling of volatile elements. *Geochem. Geophys. Geosyst.* 3, 1–29. doi: 10.1029/2001GC000173

Somoza, R., and Ghidella, M. E. (2012). Late Cretaceous to recent plate motions in western South America revisited. *Earth Planet. Sci. Lett.* 331, 152–163. doi: 10.1016/j.epsl.2012.03.003

Steiger, R. H., and Jagger, E. (1977). Subcommission on geochronology: convention on the use of decay constants in geo- and cosmochronology. *Earth Planet. Sci. Lett.* 36, 359–362. doi: 10.1016/0012-821X(77)90060-7

Steinberger, B., and Torsvik, T. H. (2012). A geodynamic model of plumes from the margins of Large Low Shear Velocity Provinces. *Geochem. Geophys. Geosyst.* 13:Q01W09. doi: 10.1029/2011GC003808

Stuessy, T. F., Foland, K. A., Sutter, J. F., Sanders, R. W., and Silva, M. (1984). Botanical and geological significance of potassium-argon dates from the Juan Fernández Islands. *Science* 225, 49–51. doi: 10.1126/science.225.4657.49

Tassara, A., Götze, H. J., Schmidt, S., and Hackney, R. (2006). Three-dimensional density model of the Nazca plate and the Andean continental margin. *J. Geophys. Res. Solid Earth* 111:B09404. doi: 10.1029/2005JB003976

Tebbens, S. F., and Cande, S. C. (1997). Southeast Pacific tectonic evolution from early Oligocene to present. *J. Geophys. Res. Solid Earth* 102, 12061–12084. doi: 10.1029/96JB02582

Tebbens, S. F., Cande, S. C., Kovacs, L., Parra, J. C., LaBrecque, J. L., and Vergara, H. (1997). The Chile ridge: a tectonic framework. *J. Geophys. Res. Solid Earth* 102, 12035–12059. doi: 10.1029/96JB02581

Truong, T. B., Castillo, P. R., Hilton, D. R., and Day, J. M. D. (2018). The trace element and Sr-Nd-Pb isotope geochemistry of Juan Fernández lavas reveal variable contributions from a high- 3He/4He mantle plume. *Chem. Geol.* 476, 280–291. doi: 10.1016/j.chemgeo.2017.11.024

Vogt, P. R., and Smoot, N. C. (1984). The Geisha Guyots: multibeam bathymetry and morphometric interpretation. *J. Geophys. Res. Solid Earth* 89, 11085–11107. doi: 10.1029/JB089iB13p11085

von Huene, R., Corvalán, J., Flueh, E. R., Hinz, K., Korstgard, J., Ranero, C. R., et al. (1997). Tectonic control of the subducting Juan Fernández Ridge on the Andean margin near Valparaiso, Chile. *Tectonics* 16, 474–488. doi: 10.1029/96TC03703

Wang, S., Yu, H., Zhang, Q., and Zhao, Y. (2018). Absolute plate motions relative to deep mantle plumes. *Earth Planet. Sci. Lett.* 490, 88–99. doi: 10.1016/j.epsl.2018.03.021

Weatherall, P., Marks, K. M., Jakobsson, M., Schmitt, T., Tani, S., Arndt, J. E., et al. (2015). A new digital bathymetric model of the world's oceans. *Earth Space Sci.* 2, 331–345. doi: 10.1002/2015EA000107

Wessel, P., and Smith, W. H. F. (1995). New version of the Generic Mapping Tools released. *EOS Trans. Am. Geophys. Union* 76:329. doi: 10.1029/95EO00198

Wilson, J. (1963). A possible origin of the Hawaiian islands. *Can. J. Phys.* 41, 863–870. doi: 10.1139/p63-094

Yáñez, G., Cembrano, J., Pardo, M., Ranero, C., and Selles, D. (2002). The Challenger–Juan Fernández–Maipo major tectonic transition of the Nazca–Andean subduction system at 33-34 S: geodynamic evidence and implications. *J. South Am. Earth Sci.* 15, 23–38. doi: 10.1016/S0895-9811(02)00004-4

Yáñez, G. A., Ranero, C. R., Huene, R., and Díaz, J. (2001). Magnetic anomaly interpretation across the southern central Andes (32-34 S): the role of the Juan Fernández Ridge in the late Tertiary evolution of the margin. *J. Geophys. Res.* 106, 6325–6345. doi: 10.1029/2000JB900337

York, D. (1969). Least-squares fitting of a straight line. *Can. J. Phys.* 44, 1079–1086. doi: 10.1139/p66-090